

Geophysical Research Letters

RESEARCH LETTER

10.1029/2020GL089114

Key Points:

- Low-pass filtered wave- and grain-scale components of dynamic pressure gradient explain the multiscale behavior of hyporheic exchange flows
- Wave-scale pumping plays a predominant role over grain-scale pumping in hyporheic exchange flows especially with increasing stream discharge
- Current-induced phase lag suggests a shift from the existing water surface-based wave pumping model to a pressure gradient-based approach

Supporting Information:

- Supporting Information S1
- Movie S1
- Movie S2
- Movie S3
- Table S1
- Table S2
- Table S3

Correspondence to:

F.-C. Wu,
fcwu@ntu.edu.tw

Citation:

Shih, W. R., & Wu, F.-C. (2020). Hyporheic exchange under undular flows over a coarse granular bed. *Geophysical Research Letters*, 47, e2020GL089114. <https://doi.org/10.1029/2020GL089114>

Received 31 MAY 2020

Accepted 4 AUG 2020

Accepted article online 18 AUG 2020

Hyporheic Exchange Under Undular Flows Over a Coarse Granular Bed

WuRong Shih^{1,2}  and Fu-Chun Wu¹ 

¹Department of Bioenvironmental Systems Engineering and Hydrotech Research Institute, National Taiwan University, Taipei, Taiwan, ²Department of Civil Engineering, National Chung Hsing University, Taichung, Taiwan

Abstract Undular flows over riffles (standing waves with underlying open-channel flows) facilitate a quality environmental setting for riverine habitats. Understanding their link with hyporheic exchange flow (HEF) is important from eco-hydro-geomorphic perspectives. We conduct refractive index-matched scanning experiments to resolve the exchange between surface and subsurface flows across a coarse granular bed. We show that the HEF includes wave pumping (WP) and grain-scale pumping (GP) components. Mechanistically, the dynamic pressure gradient best explains the HEF on both wave and grain scales. However, due to the underlying open-channel flow, the result exhibits a phase lag compared to the theoretical WP, suggesting a necessary shift from the existing water surface-based model to a pressure gradient-based approach. Quantitatively, with the present experimental setting, the GP flux is 1 order of magnitude smaller than the WP flux. The relative significance of WP to GP is further increased at higher discharges, indicating potential utility of WP in habitat vitalization.

1. Introduction

Hyporheic exchange, based on a hydrodynamic definition, occurs in a surface or subsurface area that contains the flow lines across the sediment-water interface (Gomez-Velez et al., 2017; Gooseff, 2010; Wu et al., 2018). Hyporheic exchange has long been recognized for its importance to aquatic ecology and biogeochemistry (Boano et al., 2014; Tonina & Buffington, 2009). Hyporheic exchange flows (HEFs) can be driven by interfacial pressure gradients induced by local channel steepening (e.g., riffles, steps), flow transition (e.g., large boulders, logs, instream structures), flow separation and reattachment (e.g., dunes, ripples), surface waves, or substrate heterogeneity (e.g., permeability); it may also be driven by near-bed turbulence or turnover of bedforms (e.g., Blois et al., 2014; Buffington & Tonina, 2009; Cardenas & Wilson, 2007; Clark et al., 2019; Elliott & Brooks, 1997; Endreny et al., 2011; Hester & Doyle, 2008; Higashino et al., 2009; Lichtner, 2015; Packman et al., 2004; Qian et al., 2008; Roche et al., 2018; Sawyer et al., 2011; Sawyer & Cardenas, 2009). In this study, we focus on vertical HEFs across a flat bed without bedforms, driven by pressure gradients of undular flows, which are a combination of free-surface flows and standing waves. A modeling study of solute exchange in a similar setting has been conducted previously (Qian et al., 2008); here we use an experimental approach to study the hydrodynamics of hyporheic flows. Flows beneath the standing waves are characterized by vortices and a distribution of dynamic pressure that is distinct from its hydrostatic counterpart described by local water surface elevation (Tonina & Buffington, 2007). The hydrostatic pressure acts to counteract the gravity such that a static fluid is in a state of equilibrium (Constantin, 2016), which motivates us to decompose the pressure beneath a surface wave as a dynamic part that drives the fluid motion and a hydrostatic part due to the weight of the fluid. Hereinafter, pressure thus refers to the dynamic part excluding the effect of gravity.

Riffles are ubiquitous mesoscale bedforms and important habitats in gravel-bed streams (Hose et al., 2005; Jowett & Richardson, 1995; Newson & Newson, 2000). Under regular low discharges, the surface flows over riffles are characterized by stationary undulations, often called standing waves (see Figure 1a and Movie S1) (Tonina & Buffington, 2007; Trauth et al., 2013). Such flows occur following an undular hydraulic jump where the flow passes the downslope patch of the riffle with its Froude number Fr being slightly >1 and enters the head of the pool where Fr is <1 (Chanson, 1996; Dey et al., 2013; Gotoh et al., 2005). These flows also exhibit low relative submergence (i.e., ratio of water depth to grain size <10) (Ferguson, 2007). Although it is well known that the mesoscale hyporheic flows across the upslope and downslope faces of the riffle are

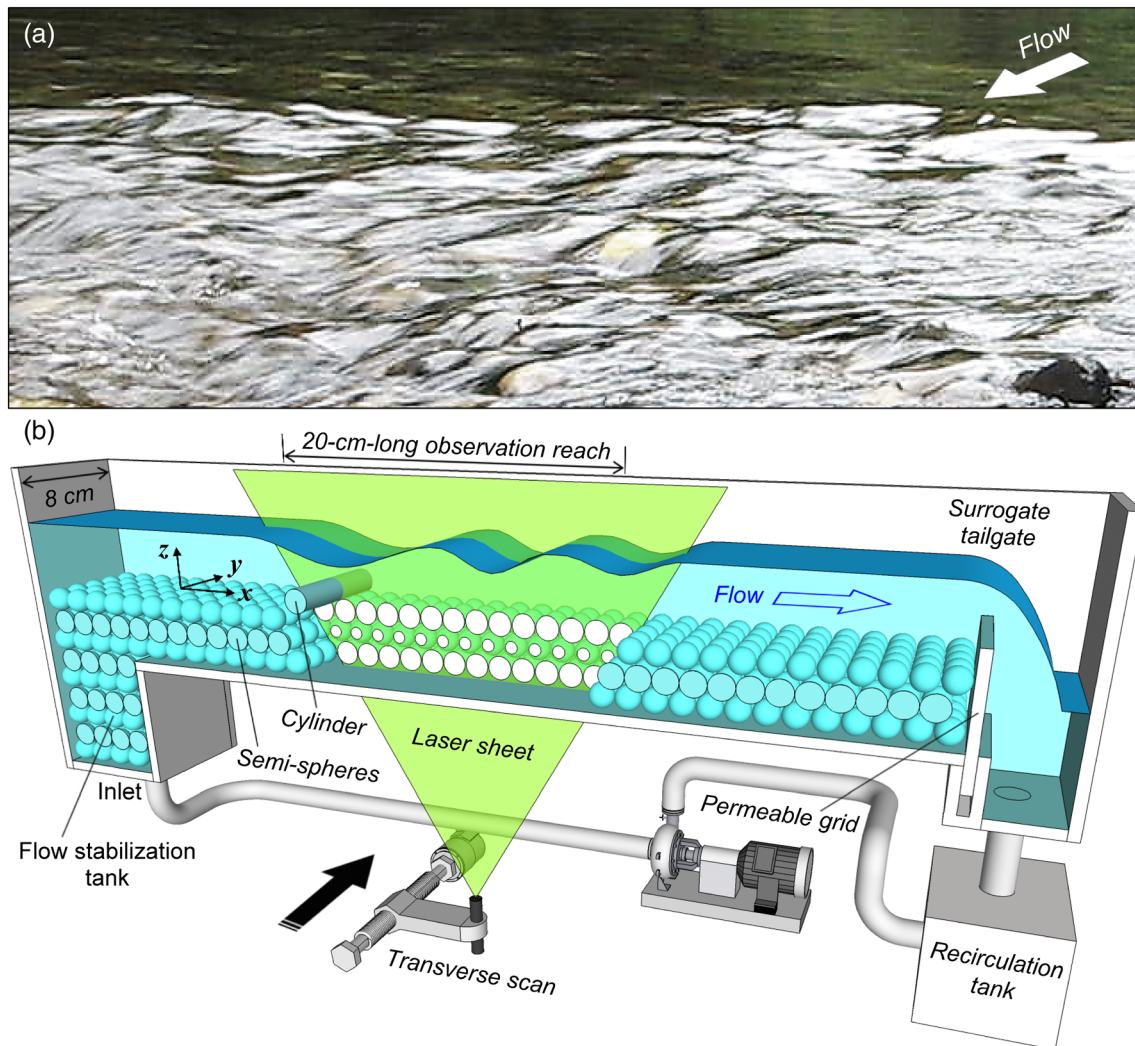


Figure 1. (a) Undular flow over riffle, observed at upper Tong-Hou Creek in northern Taiwan (see also Movie S1). The bed slope over this patch was 1.5%. The relative submergence was low, with ratios of flow depth to grain size ranging from 0.7 to 2.1 (average of 1.6). The wave steepness (ratio of wave amplitude to wavelength) ranged from 0.025 to 0.075, with an average of 0.045. (b) Schematic plot of experimental setup: RIM scanning of surface and subsurface flow fields (see Text S1 for photos).

driven by pressure gradients induced by spatial variations of water surface elevation, the effect of the patch-scale standing waves on HEFs is still poorly understood (Tonina & Buffington, 2007).

Previous studies on the wave-induced hyporheic exchange have postulated a wave pumping mechanism governed by a sinusoidal pressure wave in phase with the surface waves (Habel & Bagtzoglou, 2005; Huettel & Webster, 2001; King et al., 2009; Precht & Huettel, 2003; Qian et al., 2008, 2009; Riedl et al., 1972). By such mechanism, the positive vertical pressure gradients under wave crests drive the surface water into the bed, whereas the negative pressure gradients under wave troughs expel the water from the bed. These wave pumping models, however, build on the potential flow solution for irrotational waves, neglecting the influence of the underlying current (open-channel flow), and aim for cases with horizontal, flat beds composed of fine sediment. Their validity for undular flows over sloping, coarse granular beds has yet to be examined. Moreover, it has been reported that the grain-scale topography and high permeability of the coarse granular beds would give rise to additional advective pumping flows associated with local flow separation and reattachment between adjacent grains (Clark et al., 2019; Packman et al., 2004; Pokrajac & Manes, 2009).

Herein, with the patch-scale riffle hydrodynamics in mind, we aim to (1) investigate whether the existing wave pumping model explains the hyporheic exchange under undular flows over a sloping, coarse granular bed and (2) assess the relative importance of grain-scale advective pumping flow to patch-scale wave pumping flow. To this aim, simultaneous characterizations of hyporheic fluxes and interfacial pressure gradients, a novel experimental task, are pursued here. We conduct experiments using undular open-channel flows over a granular bed packed with identical spheres. Recent experimental studies have shown that refractive index-matched (RIM) techniques are effective for mapping the surface and subsurface flow fields in uniform open-channel flows (Kim et al., 2018; Voermans et al., 2017). By using the RIM solid and liquid to make the granular bed transparent, we capture flow fields on both sides of the interface, coupled with the particle tracking velocimetry (PTV) to gain optical access to the internal subsurface flow. To account for the spatial heterogeneity, we use a laser sheet to scan the flow transversely, and the results are integrated temporally and spatially under a double-averaging analysis framework. In a more dynamic setting, Ni and Capart (2018) acquired longitudinal and transverse scans to resolve the internal solid and liquid motions of turbulent bedload layers in uniform open-channel flows. Here, we apply the RIM scanning to undular flows, aimed to unravel the driving mechanisms and the multiscale behaviors of HEF.

2. Experiments

Design of the experiments obeyed the law of similitude. For geometric similarity, the channel slope S , relative submergence (ratio of flow depth h to grain size d), and wave steepness (ratio of wave amplitude a to wavelength λ) were selected to resemble those of natural riffles and the overlying undular flows. For dynamic similarity, the pre- and post-jump Froude numbers $Fr (= U/\sqrt{gh})$, where U is depth-averaged free-stream velocity and g is gravitational acceleration) should resemble those before and after natural undular hydraulic jumps, and the permeability Reynolds numbers $Re_K (= u_*\sqrt{K}/\nu)$, where $u_* = \sqrt{ghS}$ is shear velocity, $K = n^3d^2/180(1-n)^2$ is sediment permeability, n is porosity, and ν is fluid viscosity) were adjusted to properly replicate the natural stream settings (Voermans et al., 2017). The experimental and field values of these parameters are summarized in Table S1.

The RIM materials used were solid spheres made of polymethyl metacrylate (PMMA) and the organic liquid para-cymene (Haam et al., 2000), with the closest match of refractive index ($=1.49$) attained at temperatures near 17°C. Spheres of diameter 16 mm were used, which secured the low relative submergence ($h/d < 10$) and the permeability Reynolds numbers commonly encountered in natural riffles. The liquid has density $\rho = 855 \text{ kg/m}^3$ and kinematic viscosity $\nu = 1.2 \times 10^{-6} \text{ m}^2/\text{s}$, seeded with 50- μm tracer particles. Two experiments, Exp. 1 and 2, were conducted in a recirculating channel of length 110 cm and width 8 cm, with transparent walls and floor made of PMMA (see Figure 1b and Text S1). The channel accommodated a 50-cm entrance length to develop turbulent flows, followed by a 20-cm observation reach, located 40 cm from the downstream end to alleviate boundary effects. The slope was 1.4% and 1.2% in Exp. 1 and 2, typical values for natural riffles (Jowett, 1993). The wavelength in Exp. 1 was longer, and only one cycle of wave crest and trough was present in the observation reach; Exp. 2 was aimed for a shorter wavelength such that more wave cycles could be observed. The granular bed was closest packed with three layers of spheres. In the top and bottom layers, the width of the channel allowed five full spheres; in the middle layer were four full spheres with a semi-sphere attached to each sidewall, restricting the otherwise preferential flow through the greater voids on both sides. Liquid discharges, 0.78 and 0.39 L/s in Exp. 1 and 2, were set by varying the pump flow rate. Above the inlet was a tank containing multiple layers of spheres for flow straightening. A permeable grid was used at the downstream end to hold the granular bed, which imposed minimal disturbance to the subsurface flow. A surrogate tailgate was used for flow depth adjustment attaining quasi-uniform flows.

A channel-spanning cylinder of diameter 16 mm (same as sphere size) was placed on the bed at 50 cm from the inlet to create a rapid transition to supercritical flow (with Fr slightly > 1), followed by a hydraulic jump and subcritical undular flow with a sequence of standing waves that attenuated downstream. The resulting wave steepness (0.03) was within the range observed in the field, and the permeability Reynolds numbers (9.7 and 8.1) resembled those of natural permeable beds (Voermans et al., 2017). Hyporheic flows were induced by both the cylinder and standing waves, and a normalized declining trend (NDT) approach was

devised to separate their individual contributions (section 4.4). The observation area covered the surface and subsurface flow regions downstream of the cylinder. Flows were scanned transversely from below at a speed v_{LS} , imaged from the right with a high-speed camera operated at 300 frames per second (fps). The laser plane was oriented parallel to the flow, scanned from $y = -16$ to 16 mm ($y = 0$ at the centerline of the channel) covering two cycles of sphere crest and trough, with the camera perspective orthorectified by the calibrated transformations (Ni & Capart, 2015). For each experiment, nine repeated scans were conducted, yielding more than 50,000 images. All images were preprocessed and then used to track the paths of the tracer particles and reconstruct the instantaneous velocity fields of in-plane streamwise and vertical components (u , w), using the PTV procedure described in Text S2 (see also Movie S2 for intermediate products).

3. Double-Averaging Approach

3.1. Velocity and Pressure Fields

As the transverse scans captured the flow fields at different locations of y , the acquired velocity fields exhibited a spatial variability arising from highly heterogeneous grain-scale topography and pore geometry of the granular bed. To account for such variability, the scanned volume is laterally split into 33 slices, each with a thickness $\Delta y = 1$ mm centered about an integer y_n ($= -16$ to 16 mm). Within each slice, the instantaneous velocity fields $\mathbf{V}(x, y, z, t)$ are averaged over Δt or Δy ($= v_{LS} \Delta t$) to yield the local time-averaged velocity field $\bar{\mathbf{V}}(x, y_n, z)$, with $\mathbf{V} = (u, w)$ and $\bar{\mathbf{V}} = (\bar{u}, \bar{w})$ being the instantaneous and time-averaged velocity vectors. The relation between the instantaneous and time-averaged velocity fields follows the Reynolds decomposition:

$$\mathbf{V}(x, y, z, t) = \bar{\mathbf{V}}(x, y_n, z) + \mathbf{V}'(x, y, z, t) \quad (1)$$

where $\mathbf{V}' = (u', w')$ are turbulent velocity fluctuations, by definition $\bar{\mathbf{V}}' = \mathbf{0}$. The local time-averaged velocity fields $\bar{\mathbf{V}}(x, y_n, z)$ are then averaged over y_n (from -16 to 16 mm) to yield the time-space double-averaged velocity field $\langle \bar{\mathbf{V}} \rangle(x, z)$, with $\langle \bar{\mathbf{V}} \rangle = (\langle \bar{u} \rangle, \langle \bar{w} \rangle)$ being the double-averaged velocity vectors. The relation between the time-averaged and double-averaged velocity fields is given by

$$\bar{\mathbf{V}}(x, y_n, z) = \langle \bar{\mathbf{V}} \rangle(x, z) + \tilde{\mathbf{V}}(x, y_n, z) \quad (2)$$

where $\tilde{\mathbf{V}} = (\tilde{u}, \tilde{w})$ are spatial velocity disturbances, by definition $\langle \tilde{\mathbf{V}} \rangle = \mathbf{0}$.

The concepts of time averaging and double averaging can be applied also to the pressure fields. The local time-averaged pressure field can be determined by integrating the pressure divergence term in the Navier-Stokes equation for the time-averaged velocity field of incompressible fluid, expressed in vector form as follows:

$$\bar{\nabla} \cdot \bar{p} = -\rho \left(\frac{D\bar{\mathbf{V}}}{Dt} - \nu \nabla^2 \bar{\mathbf{V}} \right) \quad (3)$$

where $\bar{\nabla} \cdot \bar{p}$ is the divergence of time-averaged dynamic pressure; $D\bar{\mathbf{V}}/Dt$ is the material derivative of time-averaged velocity; $\nabla^2 \bar{\mathbf{V}}$ is the Laplacian of time-averaged velocity; and ρ and ν are fluid density and kinematic viscosity. Direct integration of Equation 3 from point $\mathbf{x}_1 = (x_1, z_1)$ to $\mathbf{x}_2 = (x_2, z_2)$ yields the pressure difference between the two points:

$$\bar{p}_2 - \bar{p}_1 = \int_{\mathbf{x}_1}^{\mathbf{x}_2} \bar{\nabla} \cdot \bar{p} \cdot d\mathbf{x} \quad (4)$$

With a number of independent integration paths, the local pressure at a given point can be evaluated using the median-based algorithm presented by Dabiri et al. (2014). Similar to the double averaging of velocity fields, the time-averaged pressure fields of individual slices $\bar{p}(x, y_n, z)$ so determined are then averaged over y_n to yield the double-averaged pressure field $\langle \bar{p} \rangle(x, z)$.

3.2. Contributors to Hyporheic Flux

To apply the double-averaging framework to the surface flow region ($z \geq z_c$), we highlight below the vertical (i.e., z direction) component of the double-averaged Navier-Stokes (DANS) equation for steady flows (Giménez-Curto & Corniero Lera, 1996; Nikora et al., 2001):

$$\langle \bar{u} \rangle \frac{\partial \langle \bar{w} \rangle}{\partial x} + \langle \bar{w} \rangle \frac{\partial \langle \bar{w} \rangle}{\partial z} = \frac{-1}{\rho} \frac{\partial \langle \bar{p} \rangle}{\partial z} + \nu \left[\frac{\partial^2 \langle \bar{w} \rangle}{\partial x^2} + \frac{\partial^2 \langle \bar{w} \rangle}{\partial z^2} \right] - \left[\frac{\partial \langle \bar{u}'w' \rangle}{\partial x} + \frac{\partial \langle \bar{w}'w' \rangle}{\partial z} \right] - \left[\frac{\partial \langle \bar{u}\tilde{w} \rangle}{\partial x} + \frac{\partial \langle \bar{w}\tilde{w} \rangle}{\partial z} \right] \quad (5)$$

where $\bar{u}'w'$ and $\bar{w}'w'$ are Reynolds shear and normal stresses, respectively, and $\bar{u}\tilde{w}$ and $\bar{w}\tilde{w}$ are form-induced shear and normal stresses due to spatial velocity disturbances. Given that our focus is placed on the vertical hyporheic flux across a flat bed (without bedforms), we can rearrange (5) to determine the streamwise (i.e., x direction) gradient of vertical velocity component along the interface ($z = z_c$):

$$\underbrace{\frac{\partial \langle \bar{w} \rangle}{\partial x} \Big|_{z=z_c}}_{\text{Hyporheic flux grad.}} = \left\{ \underbrace{\left[-\frac{\langle \bar{w} \rangle}{\langle \bar{u} \rangle} \frac{\partial \langle \bar{w} \rangle}{\partial z} \right]}_{\text{Convective acceleration}} + \underbrace{\frac{-1}{\rho \langle \bar{u} \rangle} \left[\frac{\partial \langle \bar{p} \rangle}{\partial z} \right]}_{\text{Pressure gradient}} + \underbrace{\frac{\nu}{\langle \bar{u} \rangle} \left[\frac{\partial^2 \langle \bar{w} \rangle}{\partial x^2} + \frac{\partial^2 \langle \bar{w} \rangle}{\partial z^2} \right]}_{\text{Viscous stresses}} + \underbrace{\frac{-1}{\langle \bar{u} \rangle} \left[\frac{\partial \langle \bar{u}'w' \rangle}{\partial x} + \frac{\partial \langle \bar{w}'w' \rangle}{\partial z} \right]}_{\text{Reynolds stresses}} + \underbrace{\frac{-1}{\langle \bar{u} \rangle} \left[\frac{\partial \langle \bar{u}\tilde{w} \rangle}{\partial x} + \frac{\partial \langle \bar{w}\tilde{w} \rangle}{\partial z} \right]}_{\text{Form stresses}} \right\} \Big|_{z=z_c} \quad (6)$$

Equation 6 indicates that the streamwise variation of vertical hyporheic flux across the interface is driven by (1) vertical convective acceleration; (2) vertical pressure gradient; and (3) viscous, Reynolds, and form stresses. All of the above terms can be evaluated from the double-averaged velocity and pressure fields, enabling us to quantify the contribution of each driver to the hyporheic exchange.

4. Results and Discussion

4.1. Velocity and Pressure Fields

The velocity and pressure fields of Exp. 1 and 2 are given in Text S3 and Figure 2, respectively. Over the cylinder, a rapid transition to supercritical flow was followed by an undular hydraulic jump and a sequence of standing waves. The wavelength in Exp. 1 was 8.8 cm, and only one cycle of wave crest and trough was present in the observation reach (Figure S4); Exp. 2 had a shorter wavelength (6.1 cm), and thus, 2.5 wave cycles were observable (Figure 2). In the subsurface region, two types of HEF were identified. The first one is the cylinder-induced hyporheic flow, characterized by the downstream-directed downwelling (DS-DW) flow beneath the cylinder and the downstream-directed upwelling (DS-UW) flow extending far downstream. As shown in Figure 2a, the lowermost streamline remained affected by the DS-UW flow beyond $x = 120$ mm. The second type of HEF is the alternate, shallow DS-DW and DS-UW flows induced by the standing waves.

Of these two types of HEF, the cylinder-induced hyporheic flow has been studied experimentally by many researchers (e.g., Endreny et al., 2011; Gordon et al., 2013; Hester & Doyle, 2008; Lichtner, 2015; Sawyer et al., 2011, 2012), yet the experimental study of wave-induced hyporheic flow has been relatively rare (Clark et al., 2019). The above-listed studies have shown that, when no hydraulic jump or standing waves were present, the DS-DW flows beneath the cylinder were followed by uniform, declining DS-UW flows. When a hydraulic jump was present, Endreny et al. (2011) observed that at the toe of the hydraulic jump, the DS-UW flows were enhanced. Our results confirmed such observation and revealed that the enhanced upwelling was attributed to the vertical pressure difference, thus pressure gradient, induced by the supercritical flow (Figures 2b and S4d). Moreover, we observed that when standing waves were present downstream of Crest 1, the alternate, shallow DS-DW and DS-UW flows arose as a result of the alternate positive and negative pressures (see section 4.2). To focus on the effect of standing waves upon the HEF and alleviate the influences of the cylinder and hydraulic jump, in this study, we restricted our analyses to the area downstream of Crest 1 (Figures 2a and S4c). To disentangle the effect of the cylinder-induced DS-UW flow that

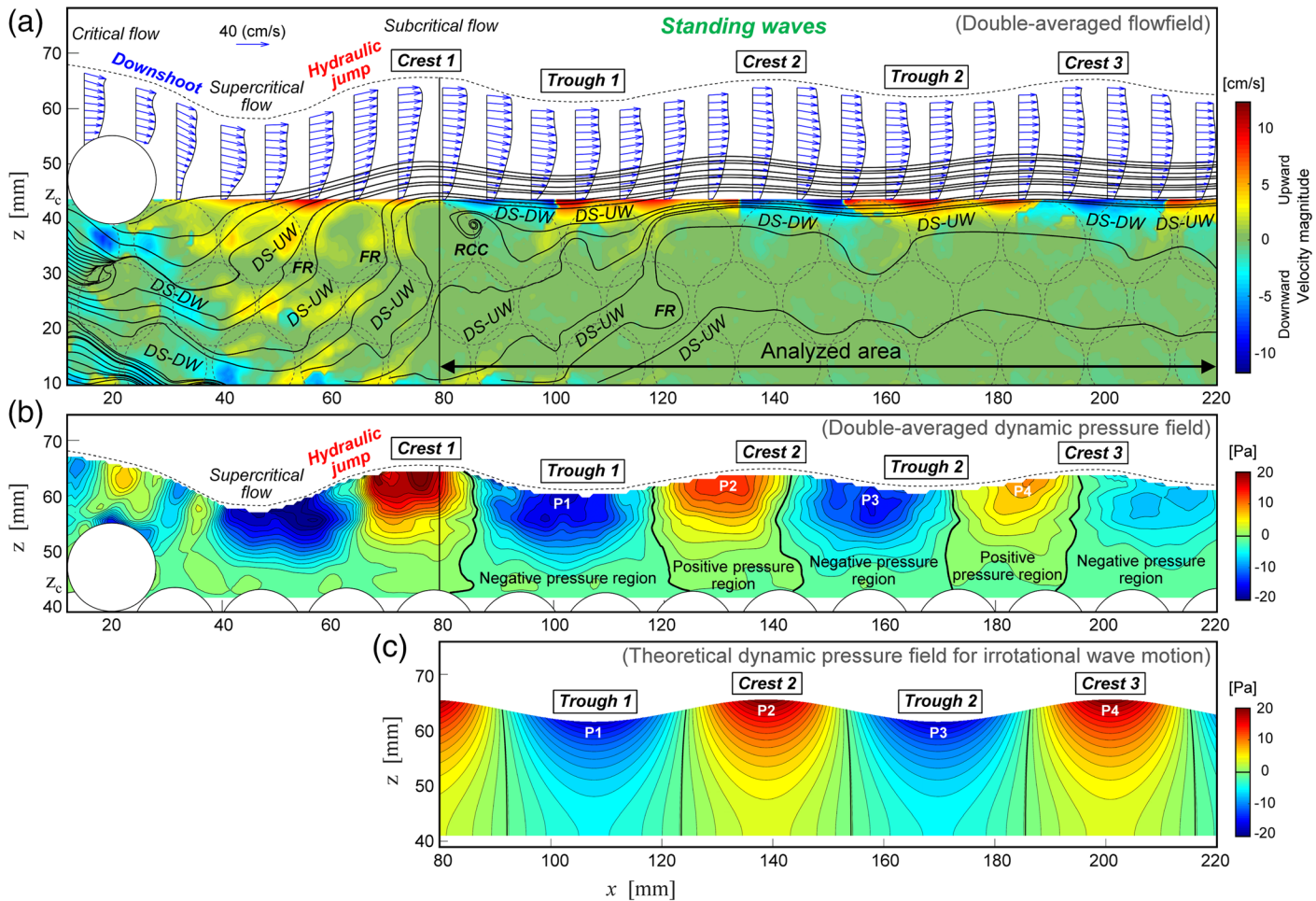


Figure 2. Exp. 2: Double-averaged (a) velocity field (with hyporheic flow streamlines) and (b) dynamic pressure field. DS-DW and DS-UW, downstream-directed downwelling and upwelling; US-DW and US-UW, upstream-directed downwelling and upwelling; RCC, reversed circulation cell; FR, flow reversal. (c) Theoretical pressure field (Tchet, 2005) used in existing wave pumping models (irrotational wave field over a flat bed with no underlying current).

remained in this area, we devised an NDT approach to isolate the individual contributions of the cylinder and standing waves (see section 4.4).

In addition to the HEF mentioned above, two localized flow patterns, as reported by Endreny et al. (2011), were observed in the subsurface. They are (1) reversed circulation cell (RCC), defined as upstream-directed downwelling (US-DW) connecting to upstream-directed upwelling (US-UW), which developed beneath Crest 1, and (2) flow reversal (FR), defined as DS-UW connecting to US-UW, which formed upstream of Crests 1 and 2. These localized flows resulted from a pair of downward and upward shear stresses arising at the junction of downwelling and upwelling flows (see Text S3).

As a comparison, Figure 2c shows the theoretical dynamic pressure field for irrotational waves over a flat bed with no underlying current; the analytical form of the potential flow solution (Tchet, 2005) is given in Text S4. The local maxima and minima of the analytical dynamic pressure occur at the wave crests and troughs, respectively. In contrast, the experimental result exhibited a phase lag in local extrema with respect to the theoretical result. The lags ranged from 6.5 (P1) to 15.6 mm (P4), with an average of 12 mm, or approximately one fifth of the wavelength. The pressure on the front face of the crest was lower than that on the rear face. The results observed in our sloping channel agree with those observed in a horizontal channel (Umeyama, 2017), suggesting that channel slope is not the cause of such phase lags. Rather, the discrepancy between the theoretical and experimental results arose from the non-zero vorticity induced by the vertical gradient of freestream velocity (Figure 2a). The wave motion became rotational due to the vorticity, which violated the irrotational assumption of the theoretical wave field and altered the spatial distribution of

dynamic pressure (Constantin, 2016; Fan et al., 2017; Swan et al., 2001; Umeyama, 2019). Nonetheless, the theoretical and experimental pressure fields exhibited a similar range of variation (from -20 to 20 Pa).

4.2. Contributors to Hyporheic Flux

Figure 3a shows the vertical pressure gradient field superimposed by three streamwise profiles of vertical velocity $\langle \bar{w} \rangle$ along different z , among which the lowermost profile is along the interface ($z = z_c$). The zero-contour lines divided the pressure gradient field into positive- and negative-value regions. In either region, the local extremum occurred below the free surface (between $z = 50$ and 60 mm) and then declining toward the interface. Mechanistically, the positive pressure gradients drove the fluid downward, characterized by the negative-slope portions of the velocity profiles, while the negative pressure gradients drove the fluid upward, characterized by the positive-slope portions of the velocity profiles. The velocity profiles attained the local extrema at locations of zero pressure gradient. These trends were universal for different z , only that the amplitudes of velocity oscillations would scale with the magnitude of local pressure gradients. These results suggest a strong link between the vertical pressure gradient and variation of vertical velocity.

Figure 3b shows the interfacial profiles of all DANS terms given in Equation 6, presenting the individual contributions of the potential drivers to vertical hyporheic flux. The streamwise gradient of hyporheic flux $\partial \langle \bar{w} \rangle / \partial x$ is in high concordance with the pressure gradient term $-\partial \langle \bar{p} \rangle / \partial z / \rho \langle \bar{u} \rangle$, suggesting a predominant role of vertical pressure gradient. The impact of the remaining drivers appeared to be minor (see Text S5 for further discussion). In short, the convective acceleration is more likely the effect of hyporheic flux rather than the cause of the flux. The influence of viscous stresses is negligible. The form stresses are the cause of the subgrain-scale fluctuations present in the local hyporheic flux gradient. Finally, flow separation and reattachment between adjacent grains generate a grain-scale turbulent structure that facilitates the vertical gradient of Reynolds normal stress to oppose the advective pumping pressure gradient.

4.3. Wave Pumping Versus Grain-Scale Advective Pumping

The above finding that pressure gradient is the dominant driver of hyporheic flux gradient is no surprise. What caught our attention were the multiscale behaviors of the hyporheic flux and pressure gradients. Variations of the hyporheic flux and pressure gradient terms in Figure 3b did not follow precisely the alternate positive and negative pressure gradient regions in Figure 3a. It is conjectured that those discrepancies stemmed from the local grain-scale oscillations superimposed on the wave-scale variation patterns. To isolate the wave- and grain-scale components of pressure gradient, we used a Butterworth low-pass digital filter (Bianchi & Sorrentino, 2007). The low-pass filter provided a smoother form of signals, removing the smaller-scale fluctuations yet retaining the larger-scale trend by passing signals with spatial scales larger than the selected cutoff scale (see Text S6 for details). This was achieved by using a three-step procedure summarized here. In Step 1, the original pressure gradient data were low-pass filtered with a cutoff scale (=grain size) characterizing the grain-scale signals, as shown in Figure 3c (black line), which filtered the smaller-scale noises yet retained the wave- and grain-scale information. In Step 2, the original data were low-pass filtered with a cutoff scale (=wavelength) characterizing the wave-scale signals. The result retained the wave-scale information (red line), which was confirmed by the profile of depth-averaged pressure (blue dashed line) that identified the general wave-induced pressure oscillations. In Step 3, the outcome of Step 2 (wave-scale component) was subtracted from the outcome of Step 1 (superimposed wave- and grain-scale components) to isolate the grain-scale component (Figure 3d). The grain-scale signals so obtained exhibited a periodic variation pattern in which the pressure gradient attained local negative extrema above the sphere crests and local positive extrema above the sphere troughs.

The close-up of near-bed pressure field (Figure 3e) reveals the grain-scale alternate pattern of positive and negative pressure spots above the sphere crests and troughs, respectively. These pressure spots are superimposed on the wave-induced background pressure field, which could thus be enhanced or concealed by the background pressures. The local negative and positive extrema of pressure gradient seen in Figure 3d correspond to the near-bed positive and negative pressure spots shown in Figure 3e. The grain-scale advective pumping has been identified as a mechanism of HEF, driven by the dynamic pressure variations induced by flow separation and reattachment between adjacent grains (Packman et al., 2004; Pokrajac & Manes, 2009). Here, we made our way in demonstration of the near-bed pressure pattern responsible for the grain-scale advective pumping.

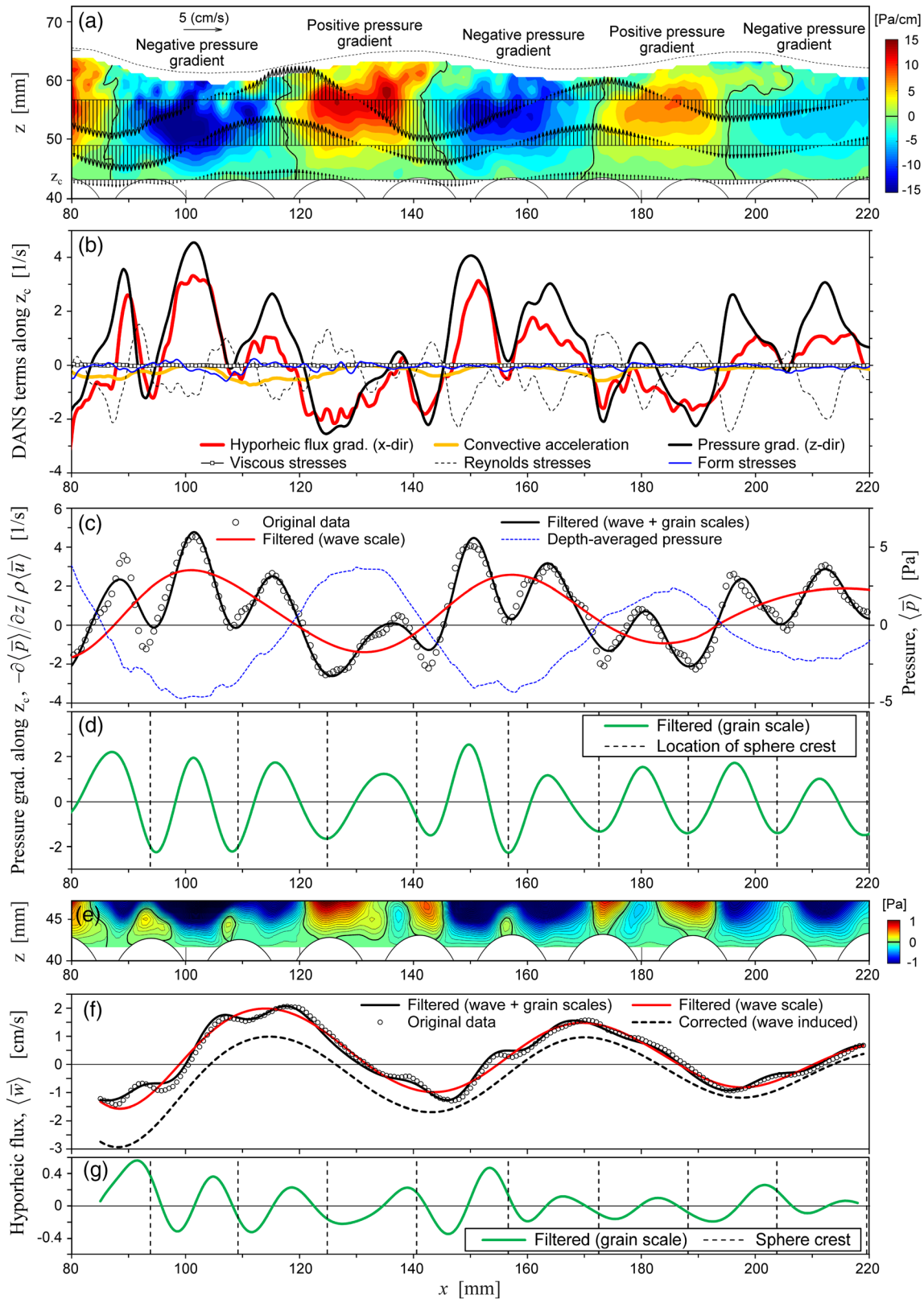


Figure 3. Exp. 2: (a) Pressure gradient field superimposed by three streamwise profiles of vertical velocity. Interfacial profiles of (b) hyporheic flux gradient and DANS terms, (c–d) original and low-pass filtered pressure gradients, and depth-averaged pressure. (e) Close-up of near-bed pressure field. (f–g) Streamwise profiles of original, low-pass filtered, and corrected vertical hyporheic fluxes.

4.4. Multiscalar Behavior of HEF

To study the multiscalar behavior of HEF, the original $\langle \bar{w} \rangle$ data were low-pass filtered to isolate the wave- and grain-scale components (red and green lines in Figures 3f and 3g). As mentioned earlier, the wave-scale hyporheic flux component so obtained is a superposition of the cylinder-induced upwelling flux and wave-induced alternate downwelling and upwelling fluxes. To disentangle the effects of cylinder and standing waves, we compared our results with those of two previous studies, in which a similar channel-spanning cylinder was used to induce hyporheic flows. The first study (Sawyer et al., 2012) used a flat sand bed ($d_{50} = 2.4$ mm). No surface waves arose due to the high relative submergence (h/d ranged from 70 to 100). The second one (Lichtner, 2015) used a coarse granular bed packed with RIM spheres of size 12.7 mm, with a lid used to prevent formation of surface waves. As the experimental settings used in these studies were rather different, a scaling is needed to factor out the differences in experimental conditions and to make the comparison more consistent, as described in the following.

Three major experimental parameters were used in the scaling. The first one being the average freestream velocity U , which represents the surface flow intensity and is used to non-dimensionalize the hyporheic flux w . The second one is the blockage ratio B , defined as the ratio of cylinder diameter D to flow depth h , which helps to quantify the effect of cylinder on hyporheic flows. The third one is the permeability Reynolds number Re_K (see section 2), a dimensionless parameter commonly used to characterize the extent of interfacial momentum transfer (Voermans et al., 2017). Incorporating these key experimental parameters would effectively minimize the differences in freestream characteristics, cylinder effect, channel slope, and sediment and fluid properties. The scaled hyporheic flux w^* is defined by a general form as $(w/U) \cdot B^{k_1} \cdot Re_K^{k_2}$, with the best-fit exponents $(k_1, k_2) = (-3, 0.4)$ for the sand bed and $(1, 0.4)$ for the coarse granular beds. The difference in k_1 is attributed to the fact that the cylinder was placed on the bed in the coarse granular-bed experiments, whereas it was placed at a small height above the bed in the sand-bed experiments.

Figure 4a shows the data from five pertinent runs in Sawyer et al. (2012), where the scaled hyporheic fluxes w^* are plotted against the scaled location x/D (the cylinder is centered at $x = 0$). These scaled data collapsed onto single curves, with the upstream downwelling flux increasing toward the cylinder yet the downstream upwelling flux declining rapidly away from the cylinder. For example, at $x/D = 7$, the upwelling flux already declined to 0.005% of $Peak_1$, with $Peak_1$ being the maximum value immediately downstream of the cylinder. In these sand-bed experiments, however, the grain-scale pumping flows were not apparent. Figure 4b shows the data from two runs in Lichtner (2015). The overall trends of downwelling and upwelling were similar to those in Figure 4a, yet two distinct features emerged. First, the hyporheic flux manifested grain-scale oscillations, with local peaks attained at sphere troughs. Second, with the 2 order of magnitude higher permeability $K = 3.3 \times 10^{-7} \text{ m}^2$ in Lichtner (2015) versus $K = 3.4 \times 10^{-9} \text{ m}^2$ in Sawyer et al. (2012), the mean declining trend of peak upwelling flow in the coarse granular bed was much milder than that observed in the sand bed. For example, at $x/D = 7$, the peak upwelling flux declined to 30% of $Peak_2$ (in contrast to 0.005% of $Peak_1$ in the sand bed).

Figure 4c shows the scaled data from this study; the wave-scale oscillations are a unique trait of our results. The negative (downwelling) fluxes at the downstream of the cylinder were unseen in Figures 4a and 4b, indicating that without wave pumping, no downwelling flows would occur. Moreover, due to the wave pumping effect, the mean declining trend of peak upwelling flow was milder than that without wave pumping (Figure 4b), and the mean declining trend of peak downwelling flow was even milder. At $x/D = 7$, for example, the peak upwelling flux declined to 44% of $Peak_3$ (in contrast to 30% of $Peak_2$ with the cylinder effect alone), and the peak downwelling flux declined more slowly to 64% of $Peak_4$. Note here that the mean declining trend of peak upwelling or downwelling flow was determined with the peak data from the analyzed areas of Exp. 1 and 2 (marked by white circles in Figure 4c), excluding those affected by the cylinder-induced downshoot and rapidly varied hydraulic jump. The grain-scale oscillations are present in Figure 4c, but much smaller than the wave-induced oscillations (see also Figures 3f and 3g). In summary, the streamwise declining of cylinder-induced upwelling was much slower in coarse granular beds than in sand beds. The declining of hyporheic flows associated with the combined cylinder-wave effect was even slower than that associated with the cylinder effect alone.

Using the mean declining trends of peak hyporheic flows given in Figures 4b and 4c, we devised an NDT approach for separating the cylinder-induced upwelling flux from the wave-induced hyporheic flux (see

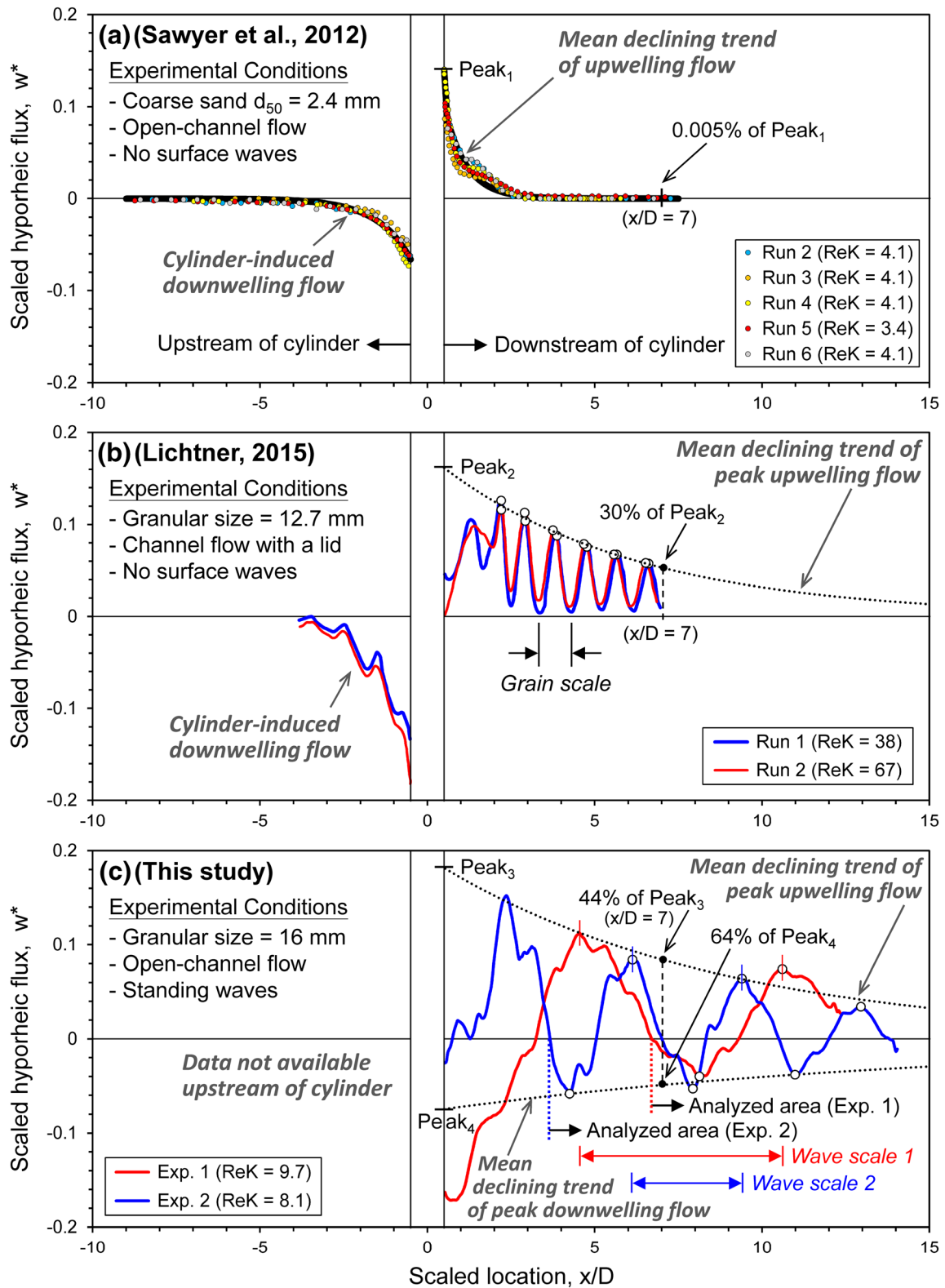


Figure 4. Scaled hyporheic flux w^* versus scaled location x/D (the cylinder is centered at $x = 0$). Source of data: (a) Sawyer et al. (2012), open-channel flow over flat coarse-sand bed with no surface waves; (b) Lichtner (2015), channel flow over coarse granular bed, with a lid used to prevent formation of surface waves; (c) this study, open-channel flow over coarse granular bed, with undular hydraulic jump and standing waves downstream of the cylinder.

Text S7 for details). The corrected profile of the wave-induced hyporheic flux is shown in Figure 3f (black dashed line), which exhibits greater downwelling than upwelling, in contrast to the original profile (red line) that exhibits greater upwelling. This transition from an upwelling-dominated profile to a downwelling-dominated one is concordant with the trend in Figure 3a, where the lowermost profile of $\langle \bar{w} \rangle$ along the interface was upwelling dominated but the uppermost profile became downwelling dominated as the latter was more distanced from the interface and less affected by the cylinder-induced upwelling.

To provide quantitative information on three types of HEF (i.e., wave-, cylinder-, and grain-induced HEFs), for each type, we calculated the total amount of hyporheic flow (per unit width) by summing the downwelling and upwelling flows, over a sufficiently long window ($x = 104$ to 213 mm) that covered two cycles of wave-induced upwelling and downwelling (see Table S3 for a summary of the results). Among these three, the total amount of wave-induced HEF ($8.59 \text{ cm}^2/\text{s}$) was the largest. The total cylinder-induced upwelling flow ($6.87 \text{ cm}^2/\text{s}$) and total grain-scale pumping flow ($1.62 \text{ cm}^2/\text{s}$) amounted 80% and 19% of the wave-induced HEF. The total amounts of wave-induced upwelling and downwelling flows comprised 34% and 66% of the total wave-induced HEF. The total upwelling and downwelling flows induced by the grain-scale advective pumping were nearly identical, indicating a balanced exchange attained by this mechanism. The results of Exp. 1, calculated over a shorter window ($x = 130$ to 200 mm), were not directly comparable to those of Exp. 2; thus, a conversion to mean flux (per unit area) was performed, as described below.

4.5. Variations of Hyporheic Fluxes With Discharge

As the discharge used in Exp. 1 was twice of that used in Exp. 2, a comparison of the results may reveal the variation trend of HEF with discharge. To facilitate such comparison, the HEFs (per unit width) were divided by the corresponding length of the hyporheic exchange region so that the resulting mean hyporheic fluxes (per unit area) were free from the length effect. Similarly, the upwelling and downwelling flows were divided by the corresponding lengths of the upwelling and downwelling regions to yield the mean fluxes. The results are described in Text S8 and summarized in Table S3. The mean fluxes for the three types of HEF invariably increased with the discharge (Figure S8a). The mean freestream flux (or velocity) U also exhibited an increasing trend. On average, the mean fluxes of wave pumping, cylinder-induced upwelling, and grain-scale pumping accounted for $\sim 4\%$, 2% , and 0.5% of the mean freestream flux. The 1 order of magnitude difference between the mean wave pumping and grain-scale pumping fluxes is consistent with the amplitudes of flux oscillations shown in Figures 3f and 3g.

We also used a freestream forcing flux ($F3$), defined as Ua/λ (a and λ are mean amplitude and wavelength of standing waves), to quantify the intensity of freestream-wave forcing. The growth ratio of $F3$ ($=F3$ at $q_{\text{Exp. 1}}/F3$ at $q_{\text{Exp. 2}}$) attained 1.62 as the unit discharge q increased from $q_{\text{Exp. 2}}$ to $q_{\text{Exp. 1}}$, or as $q/q_{\text{Exp. 2}}$ increased from 1 to 2 (Figure S8b). Among the three types of HEF, only the wave pumping flux had a growth ratio ($=2.46$) greater than that of $F3$, whereas the cylinder-induced upwelling flux and grain-scale pumping flux had growth ratios ($=1.35$ and 1.16) less than that of $F3$. As such, when normalized by the growth ratio of $F3$, only the wave pumping flux had a normalized growth ratio ($=1.52$) greater than unity, both the cylinder-induced upwelling flux and grain-scale pumping flux had their normalized growth ratios ($=0.84$ and 0.72) less than unity. With the present experimental setting, the results indicated that, as the discharge was increased by a factor of 2, the growth ratio of wave pumping flux surpassed that of $F3$ by $\sim 50\%$, whereas the growth ratios of cylinder-induced upwelling and grain-scale pumping fluxes fell behind that of $F3$ by $\sim 15\%$ and 30% . These reveal that the relative importance of wave pumping flux to grain-scale pumping flux is further increased at higher discharges.

5. Concluding Remarks

In this work, we report a first quantitative and mechanistic study on the wave- and grain-scale HEFs. In terms of mechanistic study, we show that the vertical gradient of dynamic pressure over the sediment-water interface is the dominant driver of vertical hyporheic exchange flux on both wave and grain scales. However, due to the non-zero vorticity of the underlying open-channel flow, the experimental results exhibit a phase lag with respect to the theoretical dynamic pressure distribution derived from irrotational wave field. The results thus suggest a necessary shift from the existing wave pumping model based on water surface elevation (i.e.,

downwelling under wave crests and upwelling under wave troughs) to a hydrodynamic approach based on integration of dynamic pressure gradient along the interface, as indicated by Equation 6.

In terms of quantitative study, we find that the upwelling fluxes induced by a channel-spanning cylinder are more persistent in coarse granular beds than in sand beds, and the hyporheic exchange fluxes induced by the combined cylinder-wave effect are more persistent than those induced by the cylinder effect alone. The grain-scale pumping flux is present in coarse granular beds but not in sand beds. These findings bear important implications for stream ecology. The higher persistence of hyporheic exchange fluxes in undular flows over coarse granular beds and the presence of both wave- and grain-scale hyporheic exchange fluxes make the patch-scale hydrodynamics over riffles a more favorable environmental setting for riverine habitats, for example, for nutrient cycling and metabolic waste removal (Hose et al., 2005; Jowett & Richardson, 1995), as compared to smooth surface flows over fine-grained beds. We also show that the wave pumping flux is downwelling dominated, driving more of aerated stream water into the bed, while the grain-scale pumping flux exhibits a balanced exchange between upwelling and downwelling. With the present experimental setting, the grain-scale pumping flux is 1 order of magnitude smaller than the wave pumping flux. Although both fluxes increase with discharge, the importance of wave pumping flux relative to grain-scale pumping flux is further increased at higher discharges. These results highlight the potential utility of wave pumping as an effective means of habitat vitalization.

The present study is subjected to several limitations that may be resolved in future studies. The granular bed closest packed with identical spheres can be replaced by random packed heterogeneous spheres to more closely resemble the natural gravel streambeds. The cylinder-induced undular flows can be modified by using a channel setup that includes the downslope section of a riffle connected to a pool head such that an undular hydraulic jump occurs in a more realistic way and the complicating factor of cylinder-induced upwelling flux can be excluded from the experiments. Three-dimensional subsurface flow fields may be acquired to resolve the strong transverse velocity component such that the subsurface pressure field and hyporheic flow paths can be accurately determined. Some of these tasks are currently underway.

Data Availability Statement

The data used in this study are accessible online (<http://doi.org/10.5281/zenodo.3964317>).

Acknowledgments

This study was supported by the Ministry of Science and Technology (MOST), Taiwan, with the funding granted to F. C. W. (106-2221-E-002-074-MY3, 107-2221-E-002-029-MY3, and 109-2221-E-002-012-MY3) and postdoctoral fellowship to W. R. S. (109-2811-E-002-502). We acknowledge Shih-Cheng Wu for performing the RIM scanning experiments. We thank three reviewers for critical comments that helped improve the paper.

References

- Bianchi, G., & Sorrentino, R. (2007). *Electronic filter simulation & design* (pp. 17–20). Toronto, Canada: McGraw-Hill Professional.
- Blois, G., Best, J. L., Sambrook Smith, G. H., & Hardy, R. J. (2014). Effect of bed permeability and hyporheic flow on turbulent flow over bed forms. *Geophysical Research Letters*, *41*, 6435–6442. <https://doi.org/10.1002/2014GL060906>
- Boano, F., Harvey, J. W., Marion, A., Packman, A. I., Revelli, R., Ridolfi, L., & Wörman, A. (2014). Hyporheic flow and transport processes: Mechanisms, models, and biogeochemical implications. *Reviews of Geophysics*, *52*(4), 603–679. <https://doi.org/10.1002/2012RG000417>
- Buffington, J. M., & Tonina, D. (2009). Hyporheic exchange in mountain rivers II: Effects of channel morphology on mechanics, scales, and rates of exchange. *Geography Compass*, *3*(3), 1038–1062. <https://doi.org/10.1111/j.1749-8198.2009.00225.x>
- Cardenas, M. B., & Wilson, J. L. (2007). Dunes, turbulent eddies, and interfacial exchange with permeable sediments. *Water Resources Research*, *43*, W08412. <https://doi.org/10.1029/2006WR005787>
- Chanson, H. (1996). Free-surface flows with near-critical flow conditions. *Canadian Journal of Civil Engineering*, *23*(6), 1272–1284. <https://doi.org/10.1139/196-936>
- Clark, J. J., Qian, Q., Voller, V. R., & Stefan, H. G. (2019). Hyporheic exchange in a gravel bed flume with and without traveling surface waves. *Advances in Water Resources*, *123*, 120–133. <https://doi.org/10.1016/j.advwatres.2018.11.005>
- Constantin, A. (2016). Extrema of the dynamic pressure in an irrotational regular wave train. *Physics of Fluids*, *28*(11), 113604. <https://doi.org/10.1063/1.4967362>
- Dabiri, J. O., Bose, S., Gemmill, B. J., Colin, S. P., & Costello, J. H. (2014). An algorithm to estimate unsteady and quasi-steady pressure fields from velocity field measurements. *The Journal of Experimental Biology*, *217*(3), 331–336. <https://doi.org/10.1242/jeb.092767>
- Dey, S., Bose, S. K., & Castro-Organ, O. (2013). Hydrodynamics of undular free surface flows. In P. Rowinski (Ed.), *Experimental and computational solutions of hydraulic problems, GeoPlanet: Earth and Planetary Sciences* (pp. 53–70). Berlin: Springer-Verlag. https://doi.org/10.1007/978-3-642-30209-1_3
- Elliott, A. H., & Brooks, N. H. (1997). Transfer of nonsorbing solutes to a streambed with bed forms: Theory. *Water Resources Research*, *33*(1), 123–136. <https://doi.org/10.1029/96WR02784>
- Endreny, T., Lautz, L., & Siegel, D. I. (2011). Hyporheic flow path response to hydraulic jumps at river steps: Flume and hydrodynamic models. *Water Resources Research*, *47*, W02517. <https://doi.org/10.1029/2009WR008631>
- Fan, L., Gao, H., & Mao, L. (2017). Extrema of the dynamic pressure in an irrotational Stokes wave with underlying currents and infinite depth. *Nonlinear Analysis*, *162*, 13–21. <https://doi.org/10.1016/j.na.2017.06.006>
- Ferguson, R. (2007). Flow resistance equations for gravel- and boulder-bed streams. *Water Resources Research*, *43*, W05427. <https://doi.org/10.1029/2006WR005422>

- Giménez-Curto, L. A., & Corniero Lera, M. A. (1996). Oscillating turbulent flow over very rough surfaces. *Journal of Geophysical Research*, 101(C9), 20,745–20,758. <https://doi.org/10.1029/96JC01824>
- Gomez-Velez, J. D., Wilson, J. L., Cardenas, M. B., & Harvey, J. W. (2017). Flow and residence times of dynamic river bank storage and sinuosity-driven hyporheic exchange. *Water Resources Research*, 53, 8572–8595. <https://doi.org/10.1002/2017WR021362>
- Gooseff, M. N. (2010). Defining hyporheic zones—Advancing our conceptual and operational definitions of where stream water and groundwater meet. *Geography Compass*, 4(8), 945–955. <https://doi.org/10.1111/j.1749-8198.2010.00364.x>
- Gordon, R. P., Lautz, L. K., & Daniluk, T. L. (2013). Spatial patterns of hyporheic exchange and biogeochemical cycling around cross-vane restoration structures: Implications for stream restoration design. *Water Resources Research*, 49, 2040–2055. <https://doi.org/10.1002/wrcr.20185>
- Gotoh, H., Yasuda, Y., & Ohtsu, I. (2005). Effect of channel slope on flow characteristics of undular hydraulic jumps. *WIT Transactions on Ecology and the Environment*, 83, 33–43.
- Habel, F., & Bagtzoglou, A. C. (2005). Wave induced flow and transport in sediment beds. *Journal of the American Water Resources Association*, 41(2), 461–476. <https://doi.org/10.1111/j.1752-1688.2005.tb03749.x>
- Haam, S. J., Brodkey, R. S., Fort, I., Klabocho, L., Placnik, M., & Vanecek, V. (2000). Laser Doppler anemometry measurements in an index of refraction matched column in the presence of dispersed beads: Part I. *International Journal of Multiphase Flow*, 26, 1401–1418.
- Hester, E. T., & Doyle, M. W. (2008). In-stream geomorphic structures as drivers of hyporheic exchange. *Water Resources Research*, 44, W03417. <https://doi.org/10.1029/2006WR005810>
- Higashino, M., Clark, J. J., & Stefan, H. G. (2009). Pore water flow due to near-bed turbulence and associated solute transfer in a stream or lake sediment bed. *Water Resources Research*, 45, W12414. <https://doi.org/10.1029/2008WR007374>
- Hose, G. C., Jones, P., & Lim, R. P. (2005). Hyporheic macroinvertebrates in riffle and pool areas of temporary streams in south eastern Australia. *Hydrobiologia*, 532(1–3), 81–90. <https://doi.org/10.1007/s10750-004-9016-4>
- Huettel, M., & Webster, I. (2001). Pore-water flow in permeable sediments. In B. Boudreau, & B. Jorgensen (Eds.), *The benthic boundary layer: Transport processes and biogeochemistry* (pp. 144–179). Oxford, UK: Oxford University Press.
- Jowett, I. G. (1993). A method for objectively identifying pool, run, and riffle habitats from physical measurements. *New Zealand Journal of Marine and Freshwater Research*, 27(2), 241–248. <https://doi.org/10.1080/00288330.1993.9516563>
- Jowett, I. G., & Richardson, J. (1995). Habitat preferences of common, riverine New Zealand native fishes and implications for flow management. *New Zealand Journal of Marine and Freshwater Research*, 29(1), 13–23. <https://doi.org/10.1080/00288330.1995.9516635>
- Kim, T., Blois, G., Best, J. L., & Christensen, K. T. (2018). Experimental study of turbulent flow over and within cubically packed walls of spheres: Effects of topography, permeability and wall thickness. *International Journal of Heat and Fluid Flow*, 73, 16–29. <https://doi.org/10.1016/j.ijheatfluidflow.2018.06.004>
- King, J. N., Mehta, A. J., & Dean, R. G. (2009). Generalized analytical model for benthic water flux forced by surface gravity waves. *Journal of Geophysical Research*, 114, C04004. <https://doi.org/10.1029/2008JC005116>
- Lichtner, D. T. (2015). *Turbulent interactions between stream flow and near-subsurface flow: A laboratory approach using particle image velocimetry and refractive index matching*. University of Illinois at Urbana-Champaign, USA: M.S. thesis. <http://hdl.handle.net/2142/88076>
- Newson, M. D., & Newson, C. L. (2000). Geomorphology, ecology and river channel habitat: Mesoscale approaches to basin-scale challenges. *Progress in Physical Geography*, 24(2), 195–217. <https://doi.org/10.1177/030913330002400203>
- Ni, W.-J., & Capart, H. (2015). Cross-sectional imaging of refractive-index-matched liquid-granular flows. *Experiments in Fluids*, 56(8), 163. <https://doi.org/10.1007/s00348-015-2034-3>
- Ni, W.-J., & Capart, H. (2018). Stresses and drag in turbulent bed load from refractive index-matched experiments. *Geophysical Research Letters*, 45, 7000–7009. <https://doi.org/10.1029/2018GL077571>
- Nikora, V., Goring, D., McEwan, I., & Griffiths, G. (2001). Spatially averaged open-channel flow over rough bed. *Journal of Hydraulic Engineering*, 127(2), 123–133. [https://doi.org/10.1061/\(ASCE\)0733-9429\(2001\)127:2\(123\)](https://doi.org/10.1061/(ASCE)0733-9429(2001)127:2(123))
- Packman, A. I., Salehin, M., & Zaramella, M. (2004). Hyporheic exchange with gravel beds: Basic hydrodynamic interactions and bedform-induced advective flows. *Journal of Hydraulic Engineering*, 130(7), 647–656. [https://doi.org/10.1061/\(ASCE\)0733-9429\(2004\)130:7\(647\)](https://doi.org/10.1061/(ASCE)0733-9429(2004)130:7(647))
- Pokrajac, D., & Manes, C. (2009). Velocity measurements of a free-surface turbulent flow penetrating a porous medium composed of uniform-size spheres. *Transport in Porous Media*, 78(3), 367–383. <https://doi.org/10.1007/s11242-009-9339-8>
- Precht, E., & Huettel, M. (2003). Advective pore-water exchange driven by surface gravity waves and its ecological implications. *Limnology and Oceanography*, 48(4), 1674–1684. <https://doi.org/10.4319/lo.2003.48.4.1674>
- Qian, Q., Voller, V. R., & Stefan, H. G. (2008). A vertical dispersion model for solute exchange induced by underflow and periodic hyporheic flow in a stream gravel bed. *Water Resources Research*, 44, W07422. <https://doi.org/10.1029/2007WR006366>
- Qian, Q., Voller, V. R., & Stefan, H. G. (2009). Modeling of vertical solute dispersion in a sediment bed enhanced by wave-induced interstitial flow. *Journal of the American Water Resources Association*, 45(2), 343–354. <https://doi.org/10.1111/j.1752-1688.2008.00297.x>
- Riedl, R. J., Huang, N., & Machan, R. (1972). The subtidal pump: A mechanism of interstitial water exchange by wave action. *Marine Biology*, 13(3), 210–221. <https://doi.org/10.1007/BF00391379>
- Roche, K. R., Blois, G., Best, J. L., Christensen, K. T., Aubeneau, A. F., & Packman, A. I. (2018). Turbulence links momentum and solute exchange in coarse-grained streambeds. *Water Resources Research*, 54, 3225–3242. <https://doi.org/10.1029/2017WR021992>
- Sawyer, A. H., & Cardenas, M. B. (2009). Hyporheic flow and residence time distributions in heterogeneous cross-bedded sediment. *Water Resources Research*, 45, W08406. <https://doi.org/10.1029/2008WR007632>
- Sawyer, A. H., Cardenas, M. B., & Buttles, J. (2011). Hyporheic exchange due to channel-spanning logs. *Water Resources Research*, 47, W08502. <https://doi.org/10.1029/2011WR010484>
- Sawyer, A. H., Cardenas, M. B., & Buttles, J. (2012). Hyporheic temperature dynamics and heat exchange near channel-spanning logs. *Water Resources Research*, 48, W01529. <https://doi.org/10.1029/2011WR011200>
- Swan, C., Cummins, I. P., & James, R. L. (2001). An experimental study of two-dimensional surface water waves propagating on depth-varying currents. Part 1. Regular waves. *Journal of Fluid Mechanics*, 428, 273–304. <https://doi.org/10.1017/S002211200002457>
- Techet, A. H. (2005). *Free surface water waves, Reading #7, Hydrodynamics*. Cambridge, MA: Massachusetts Institute of Technology. MIT Open Course Ware. <https://ocw.mit.edu/courses/mechanical-engineering/2-016-hydrodynamics-13-012-fall-2005/index.htm>
- Tonina, D., & Buffington, J. M. (2007). Hyporheic exchange in gravel bed rivers with pool-riffle morphology: Laboratory experiments and three-dimensional modeling. *Water Resources Research*, 43, W01421. <https://doi.org/10.1029/2005WR004328>
- Tonina, D., & Buffington, J. M. (2009). Hyporheic exchange in mountain rivers I: Mechanics and environmental effects. *Geography Compass*, 3(3), 1063–1086. <https://doi.org/10.1111/j.1749-8198.2009.00226.x>

- Trauth, N., Schmidt, C., Maier, U., Vieweg, M., & Fleckenstein, J. H. (2013). Coupled 3-D stream flow and hyporheic flow model under varying stream and ambient groundwater flow conditions in a pool-riffle system. *Water Resources Research*, *49*, 5834–5850. <https://doi.org/10.1002/wrcr.20442>
- Umeyama, M. (2017). Dynamic-pressure distributions under Stokes waves with and without a current. *Philosophical Transactions of the Royal Society A*, *376*(2111), 20170103. <https://doi.org/10.1098/rsta.2017.0103>
- Umeyama, M. (2019). Velocity and pressure in rear-end collisions between two solitary waves with and without an underlying current. *Journal of Mathematical Fluid Mechanics*, *21*(3), 37. <https://doi.org/10.1007/s00021-019-0442-5>
- Voermans, J. J., Ghisalberti, M., & Ivey, G. N. (2017). The variation of flow and turbulence across the sediment-water interface. *Journal of Fluid Mechanics*, *824*, 413–437. <https://doi.org/10.1017/jfm.2017.345>
- Wu, L., Singh, T., Gomez-Velez, J., Nützmann, G., Wörman, A., Krause, S., & Lewandowski, J. (2018). Impact of dynamically changing discharge on hyporheic exchange processes under gaining and losing groundwater conditions. *Water Resources Research*, *54*, 10,076–10,093. <https://doi.org/10.1029/2018WR023185>

References From the Supporting Information

- Giménez-Curto, L. A., & Corniero, M. A. (2002). Flow characteristics in the interfacial shear layer between a fluid and a granular bed. *Journal of Geophysical Research*, *107*(C5), 3044. <https://doi.org/10.1029/2000JC000729>
- Lengani, D., Simoni, D., Ubaldi, M., Zunino, P., & Bertini, F. (2017). Analysis of the Reynolds stress component production in a laminar separation bubble. *International Journal of Heat and Fluid Flow*, *64*, 112–119. <https://doi.org/10.1016/j.ijheatfluidflow.2017.03.001>
- Nokes, R. (2019). *Streams, Version 3.02*. University of Canterbury. <https://www.canterbury.ac.nz/engineering/schools/cnre/software/streams>
- Vision Research, Inc. (2018). *Phantom CineViewer, Version 3.1*. <https://www.phantomhighspeed.com/resourcesandsupport/phantom-resources/pccsoftware>